Advanced Electronic Materials

ADVANCED ELECTRONIC MATERIALS Open Access

www.advelectronicmat.de

RESEARCH ARTICLE OPEN ACCESS

Modeling and Characterization of Plasma Tubes as Building Blocks for Reconfigurable and Programmable Metasurfaces

Mirko Barbuto[1,8] | Alessio Monti[1] | Stefano Vellucci[2,8] | Mohammad G. H. Alijani[1] | Tonino Giagnacovo[5] | Giulia Laghi[3] | Filippo Capelli[4] | Mariachiara Grande[3] | Odhisea Gazeli[3] | Ioannis Katsantonis[6] | Jiaruo Yan[6] | Konstantinos Kourtzanidis[6,7] | Roberto Filippone[5] | Giulia Di Iorio[5] | Alessio Di Iorio[5] | Maria Kafesaki[6,9] | Matteo Gherardi[3] | Alessandro Toscano[1,8] | Filiberto Bilotti[1,8]

[1]Roma Tre University, Rome, Italy | [2]Niccolò Cusano University, Rome, Italy | [3]Alma Mater Studiorum - Università di Bologna, Bologna, Italy | [4]AlmaPlasma srl, Bologna, Italy | [5]Alma Sistemi srl, Rome, Italy | [6]Foundation for Research and Technology Hellas (FORTH), Heraklion, Crete, Greece | [7]Chemical Process & Energy Resources Institute (CPERI), Centre for Research and Technology Hellas (CERTH), Thermi, Thessaloniki, Greece | [8]Metamorphose VI AISBL, Louvain-la-Neuve, Belgium | [9]University of Crete, Heraklion, Greece

Correspondence: Mirko Barbuto (mirko.barbuto@uniroma3.it) | Filiberto Bilotti (filiberto.bilotti@uniroma3.it)

Received: 4 September 2025 | **Revised:** 30 October 2025 | **Accepted:** 18 November 2025

Keywords: electron density characterization | low-temperature plasma | plasma model | reconfigurable metasurfaces

ABSTRACT

Reconfigurable and programmable metasurfaces require reliable strategies for dynamic control of their electromagnetic response. Among the approaches explored so far, low-temperature plasma is particularly attractive thanks to its tunable permittivity, which can be adjusted in real time via electron density modulation. Despite this potential, quantitative experimental validation at microwave frequencies has remained limited. In this work, we present a comprehensive characterization of plasma tubes as reconfigurable building blocks for metasurface architectures. Using a custom waveguide measurement setup, we retrieve key plasma parameters–such as electron density and plasma frequency–under varying excitation conditions. These measurements are complemented by multiphysics plasma simulations, full-wave electromagnetic modeling, and circuit-level electrical diagnostics, ensuring cross-validation across independent methodologies. Our results demonstrate a continuous and controllable tunability of the plasma response, with electron densities reaching the $10^{19} m^{-3}$ range. The close agreement between experiments, models, and simulations confirms the feasibility of integrating plasma elements into adaptive metasurfaces. This study establishes plasma tubes as viable dynamic meta-atoms, paving the way toward high-power, high-speed, and fully reconfigurable microwave systems.

1 | Introduction

Reconfigurable and programmable metasurfaces are reshaping the landscape of electromagnetic wave manipulation by enabling dynamic control over propagation direction, wavefronts, polarization, frequency selectivity, impedance matching, and other relevant wave characteristics. These functionalities are achieved through engineered arrays of subwavelength and ultra-thin elements, sustaining a balanced combination of electric and magnetic multipoles, and whose response can be tuned in real-time. As a result, such metasurfaces are emerging as critical enablers for next-generation technologies, including wireless communications, radar systems, and high-resolution sensing platforms [1–3].

Traditional approaches to tunable metasurfaces commonly rely on integrating lumped electronic components, such as varactor diodes, PIN switches, or MEMS actuators, into the metasurface geometry [4]. While these technologies have demonstrated practical viability, but they face critical limitations: circuit complexity,

power handling constraints, complex scalability, parasitic losses, and reduced modulation speed are all bottlenecks for large-scale or high-frequency applications. Moreover, the discrete nature of switching elements limit the achievable spatial resolution of tunability across the metasurface aperture.

To address these limitations, research has increasingly turned to material-based reconfiguration, where the electromagnetic response of the meta-atoms is modulated through the intrinsic properties of the constitutive material [5–7]. In this context, low-temperature plasma gas discharges [8] have emerged as a promising platform for achieving dynamic reconfigurability. Plasmas offer a unique advantage: their effective permittivity can be tuned in real time by controlling the electron density via external excitation, enabling broad control over wave interaction without the need for lumped elements [9].

As dispersive Drude media, plasmas can exhibit dielectric or metallic behavior depending on the operating frequency and plasma parameters. This tunability makes it suitable for various applications, including tunable absorbers, power-limiters, reflectarrays, frequency-selective surfaces, and plasma-based lenses and antennas [10–24]. Additionally, the use of plasma may also enable dynamic reconfiguration of the meta-atom's operating frequency without the need to redesign or physically alter its geometry–a level of tunability that is often difficult or impractical to achieve with conventional materials or other approaches.

Particularly attractive are plasma tubes–cylindrical enclosures filled with gas and ionized via external control lines–which serve as confined, reconfigurable dielectric or conducting elements at microwave frequencies. Indeed, as theoretically and numerically demonstrated in [25–28], plasma tubes can be employed as epsilon-negative scatterers in Huygens-type metasurfaces and metagratings, enabling dynamic phase control of transmitted waves, beam steering and focusing via controlled plasma excitation.

Despite the substantial body of experimental work on bulk plasma structures, the experimental characterization of plasma elements specifically integrated within metasurface architectures remains limited. Most of the existing studies rely heavily on idealized models or simulation-driven design, with few works presenting detailed, quantitative measurements of plasma electromagnetic behavior at relevant frequencies. This is partly due to the intrinsic multiphysics nature of the problem, which involves coupled plasma kinetics and dynamics, electromagnetism, and in some cases thermal and fluid dynamics. Moreover, key plasma parameters–such as electron density and plasma frequency–must be retrieved under varying excitation conditions, requiring complex electrical and plasma diagnostics [8, 29] and high-fidelity electromagnetic measurements.

In this work, we address this gap by focusing on the quantitative modeling and experimental characterization of plasma tubes that could serve as the elementary reconfigurable units (meta-atoms) of future reconfigurable and programmable metasurfaces. Rather than addressing the design of a complete metasurface, our goal is to develop and validate a consistent framework that correlates the plasma parameters (i.e., electron density and plasma frequency) with the electromagnetic response of individual plasma elements under realistic operating conditions. To this end, we combine experimental waveguide measurements with full-wave numerical simulations and analytical modeling to extract and validate key plasma parameters. A custom-designed WR90 waveguide testbed allows us to measure transmission and reflection coefficients of plasma tubes under variable excitation, while retrieval techniques and theoretical models (e.g., Raizer and Trusov formulations) are employed to estimate electron density and plasma frequency as functions of the discharge current. These values are compared with multi-physics simulations incorporating a Drude-like plasma model, further validating the achieved results.

Our findings reveal strong and continuous tunability of the plasma tube response, confirming the feasibility of integrating such elements in reconfigurable microwave systems. These results not only demonstrate the viability of plasma-based meta-atom elements, but also offer a pathway toward the practical realization of fully reconfigurable metadevices for high-power and high-speed applications.

The remainder of this paper is organized as follows. Section 2 presents the modeling and characterization methodology adopted in this work. It is structured into three complementary parts: a multiphysics plasma model that captures the coupled physical processes governing the plasma discharge; an electrical model that enables the estimation of plasma parameters through circuit-level diagnostics; and an electromagnetic model, which describes the plasma interaction with microwave signals through an inverse fitting process, in which full-wave finite-element method (FEM) simulations are compared to measured scattering parameters to extract the plasma frequency. In Section 3, the results of the experimental characterization and numerical modeling are presented and discussed. Finally, Section 4 summarizes the key findings and outlines future directions for the integration of plasma elements in programmable metasurface platforms.

2 | Methodology

This section describes the experimental configuration and the modeling strategies adopted for characterizing the plasma tubes. The methodology combines three complementary perspectives:

1. Multiphysics plasma modeling, to capture the coupled mechanisms governing plasma generation and to estimate electron density and plasma frequency;
2. Electrical diagnostics, to extract plasma parameters from current–voltage measurements under controlled excitation;
3. Electromagnetic modeling, to determine the plasma frequency through an inverse fitting process, in which full-wave electromagnetic FEM simulations are compared to the measured scattering parameters in a waveguide setup.

2.1 | Plasma Tube Configuration

The experimental and numerical analysis presented in this work focuses on a specific plasma tube configuration, selected as a representative test case for integration into reconfigurable metasurfaces, and shown in Figure 1. The device under test

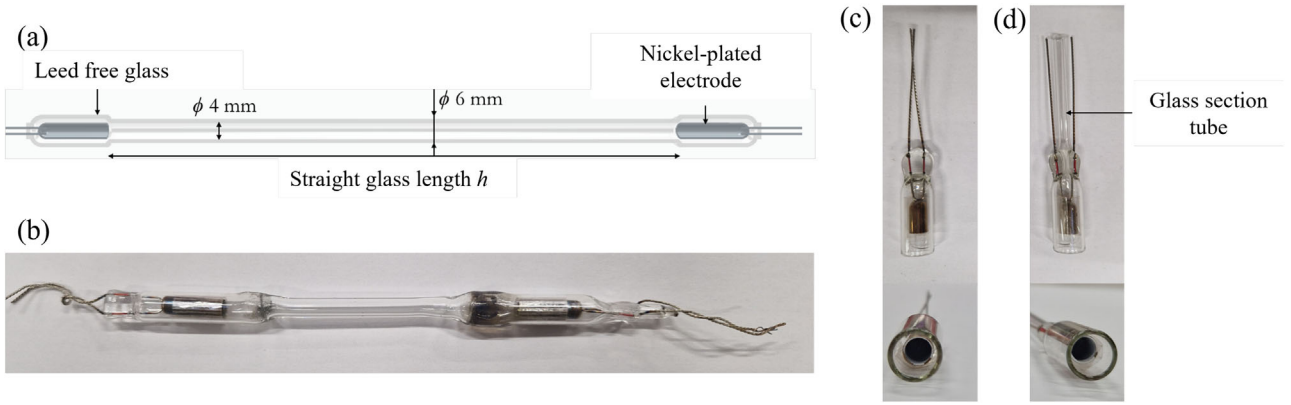

FIGURE 1 | Picture and render of the plasma tube configuration under investigation: (a) schematic and (b) photo of the entire tube; photo of the blind (c) and open (d) electrode housing.

consists of a cylindrical glass tube filled with argon at a pressure of 1 mbar. The tube features an internal diameter of 4 mm, an external diameter of 6 mm, and a total length h of 7.5 cm. Argon was selected for its favorable discharge characteristics (inert nature, low ionization energy, and ability to produce stable, uniform plasmas), while the nominal filling pressure and the geometrical parameters were selected through iterative testing and optimization to ensure stable discharge conditions and electron densities compatible with targeted reconfigurability metrics. Plasma is generated by applying a discharge current across the gas column, and its electromagnetic response is analyzed as a function of the current intensity.

In particular, our Ar plasma system is in the glow discharge regime and it is ignited through Direct Current (DC) excitation (DC discharge). DC discharge allows for a constant and more uniform in space plasma distribution compared to other excitation approaches (e.g. AC excitation). The plasma is formed within the glass tube, with the top and bottom sides of the tube bearing metallic electrodes. The electrodes, acting as anode and cathode, are connected with a power generator and are responsible for the plasma ignition and sustainability. The fabrication process includes the evacuation of air down to 0.001 mbar using a dual-stage vacuum system, followed by a conditioning phase where the tube is powered at 1.5 kW to remove residual contaminants. During this step, electrode temperatures reach 800°C instantly. The tube is then backfilled with Argon to the target pressure and hermetically sealed by melting the evacuation tube.

Having the neutral argon pressure, temperature and volume, one can easily obtain the neutral gas number density, n, employing the ideal gas law: $p = nk_BT$, where k_B is the Boltzmann constant and T is the neutral gas temperature (atmospheric temperature for our case).

We have to note here that the primary plasma sustaining mechanism in our system involves the secondary electron emission from the cathode. When ions collide with the cathode surface, there is a defined probability that they will trigger the release of electrons. These emitted electrons are then rapidly accelerated by the intense electric field near the cathode. As they gain energy, they can initiate further ionization processes. This leads to a sharp rise in electron density in the vicinity of the cathode, within a region commonly referred to as the cathode fall. On the other hand, electrons loose energy near the wall of the tube. The loss at the wall occurs due to random thermal motion, over a few mean free paths. This interplay establishes a boundary condition governing the electron flux at the plasma-glass interface.

2.2 | Plasma Electromagnetic Response and Multiphysics Modeling

It is well established that the electromagnetic response of plasma can be sufficiently accurately described by the Drude model, considering the plasma as a homogeneous and lossy free electron medium. According to the Drude model the plasma permittivity is given by [30]

$$\varepsilon_p(\omega) = \varepsilon_0\left(1 - \frac{\omega_p^2}{\omega(\omega + j\nu)}\right) \tag{1}$$

where ω is the angular frequency of the electromagnetic wave, ω_p is the plasma angular frequency, ν is the angular collision frequency, ε_0 is the vacuum permittivity, and j is the imaginary unit. The plasma permittivity is expressed as a frequency-dependent complex function, and describes how electromagnetic waves propagate through or are attenuated by the plasma medium. The parameters ω_p and ν are linked to the physical properties of the plasma, and are defined as [31]:

$$\omega_p = \sqrt{\frac{n_e e^2}{\varepsilon_0 m_e}} \tag{2}$$

$$\nu = f(p, T_e) \tag{3}$$

where n_e is the electron density (in m^{-3}), e is the elementary charge and m_e is the electron mass. The collision frequency in Equation (3) is (typically) a function of the gas pressure, p, and the electron temperature, T_e. We elaborate on the calculation of the collision frequency at the end of this section.

A simple elaboration of Equation (1) shows that the plasma permittivity becomes negative in real part for frequencies such

as $(\omega^2/\omega_p^2) < 1 - (\nu^2/\omega_p^2)$. Thus to achieve negative permittivity values in a broad spectral region the collision frequency should be sufficiently lower than the plasma frequency, dictating low pressure values. Moreover, the ratio of imaginary over real part of the susceptibility, $\chi = (\varepsilon/\varepsilon_0) - 1$, which determines the energy losses in the plasma, is equal to ν/ω, pointing also to the *requirement of low pressure values*.

From the above Formulas (1)–(3) one can see that to accurately evaluate the plasma permittivity it is essential to evaluate the electrons density of the plasma. It is also essential to evaluate the electron-neutral collision frequency, which is the dominant collision frequency term in our case (of weakly ionized gas) [8]. These quantities depend mainly on the type of gas, the neutral gas pressure, the geometry of the plasma device and the materials used (e.g. electrodes, dielectrics), as well as the electrical excitation parameters (e.g. applied voltage magnitude and frequency, type of source, discharge power).

The most fundamental way to evaluate the plasma electron density, and also electrons velocity, collision frequency and other plasma properties (e.g. velocities, rate coefficients for charged species generation and electron energy loss etc.) is to solve the Boltzmann equation (employing a continuum or a particle-based kinetic model [32]), where particles and especially electrons are represented by a distribution function, f. This approach, in conjunction with Poisson's equation, can provide essential information on the Electron Energy Distribution Function (EEDF). Having the electrons distribution function and the EEDF one can accurately obtain all the macroscopic plasma properties, such that electron density, velocity/mobility, and energy/temperature, which are the quantities that primarily determine the plasma electromagnetic response.

An alternative, yet first-principles, approach to describe plasma is to treat it macroscopically as an electrically conductive multi-species and multi-temperature fluid, based on macroscopic quantities (such as density, mean velocity, and mean energy). Such a self-consistent fluid approach captures the plasma bulk behavior very well, especially at moderate and high collisionality. Here, we employ this fluid model approach, taking into account the basic mechanisms governing the plasma formation and development, and deriving the electron density and electron energy/temperature for the Ar plasma discharge (without relying on any experimental or phenomenological parameters). The relevant simulations have been carried out employing mainly the plasma solver of COMSOL commercial software [33–35], which for DC discharges, provides a detailed implementation user-guide [36] and links to microscopic parameters determining the plasma generation and properties, such as reaction rates of the different reactions involved (obtained from the well established Phelps database [37]). Cross-checks and validations of the COMSOL results for specific cases have been made through the house-built code COPAIER [38,39].

In the model employed, the electrons are described by a continuity equation for the electron density, n_e. Similar equations describe the motion and dynamics of all charged species (all equations incorporated in the default COMSOL plasma model). In the continuity equations the drift-diffusion approximation is adopted (i.e. charged species drift under the presence of the electric field and also diffuse due to the gradients in the particles concentration), while for the evaluation of the reaction rates involved in the continuity equation the Local Mean Energy Approximation is employed. Under the Local Mean Energy Approximation all plasma transport and reaction rates depend on the mean electron energy, ϵ, which is obtained by solving a continuity-like mean electron energy density, $n_\epsilon = n_e\epsilon$, equation.

The continuity equations for the electrons density, n_e, and their mean energy density, n_ϵ, can be written as

$$\frac{\partial n_e}{\partial t} + \nabla \cdot \mathbf{\Gamma}_e = R_e \Rightarrow \frac{\partial n_e}{\partial t} + \nabla \cdot [-n_e(\mu_e \mathbf{E}) - D_e \nabla n_e] = R_e \quad (4)$$

$$\frac{\partial n_\epsilon}{\partial t} + \nabla \cdot [-n_\epsilon(\mu_\epsilon \mathbf{E}) - D_\epsilon \nabla n_\epsilon] + \mathbf{E} \cdot \mathbf{\Gamma}_e = R_\epsilon \quad (5)$$

where $\mathbf{\Gamma}_e$ is the electrons flux (electrons per unit area and time), μ_e is the electrons mobility, D_e is the electrons diffusion coefficient, μ_ϵ is the energy mobility, and D_ϵ is the energy diffusion coefficient. D_e is given by $D_e = \mu_e k_B T_e/e$ (i.e. calculated by the Einstein–Smoluchowski equation, for diffusion of charged particles; this equation for plasma particles of species s reads as $D_s = \mu_s k_B T_s/q_s$, with μ_s the mobility, T_s the temperature and q_s the charge of the particles). $\mu_\epsilon = (5/3)\mu_e$ and $D_\epsilon = (5/3)D_\epsilon$, with T_e the electron temperature [34, 35]. The electric field in the above equations is defined as $\mathbf{E} = -\nabla V$, with V being the electrostatic potential evaluated by the Poisson's equation

$$\nabla \cdot (\varepsilon_0 \varepsilon_r \nabla V) = -\rho = -\sum q_s n_s = -e \sum n_s Z_s \quad (6)$$

where the excitation parameters (e.g., applied voltage) are considered through boundary conditions. In Equation (6) ρ is the charge density. For plasma particles of species s, Z_s is the charges number, and n_s is the species' number density. In our case, the charge density of each species is automatically calculated based on the plasma chemistry.

The argon-plasma chemistry (linked to the COMSOL plasma model) includes ground-state argon, Ar, positive argon ions, Ar^+, metastable excited argon species, Ar(s), and electrons, e. We consider seven (7) reactions involved in the plasma formation, as shown in Table 1. These reactions include elastic collisions, excitation to and de-excitation, direct electron impact ionization from ground-state (R4) and from metastable state (R5), as well as metastable pooling (R6) and quenching (R7).

The electron source term in Equation (4), R_e (ionization rate per unit volume), and the R_ϵ in Equation (5), representing energy loss rate, are determined by the plasma chemistry (see Table 1) using either the conventional reaction rates or the so-called Townsend coefficients [41]. These are directly linked to COMSOL model, being obtained using the Boltzmann Equation solver under the Two-Term Approximation, with cross-sections from ref. [37]. Similar cross-sectional data have been used in ref. [42] for the electron-impact reactions of argon in simulations of DC argon/helium plasma. For DC discharges and low frequency AC discharges (i.e. 1–100 kHz frequency), where the electron flux

TABLE 1 | Chemical reactions considered (in the multiphysics model) for the Ar plasma generation and preservation. The symbol Ar(s) indicates Ar in excited state and Δ_{ε_j} is the energy loss/gain in the reaction j. The different reaction coefficients are discussed in the main text.

Reaction	Type	Δ_{ε_j} (eV)	Reaction coefficient	Reference
R1: Ar + e → Ar + e	Elastic	—	Rate coefficient, k	[33,37]
R2: Ar + e → Ar(s) + e	Excitation	11.5	Townsend coeff., a	[33,37]
R3: Ar(s) + e → Ar + e	Excitation	−11.5	Rate coeff., k	[33,37]
R4: Ar + e → Ar^+ + 2e	Ionization	15.8	Townsend coeff., a	[33,37]
R5: Ar(s) + e → Ar^+ + 2e	Ionization	4.426	Rate coeff., k	[33,37]
R6: Ar(s) + Ar(s) → Ar + Ar^+ + e	Pooling	—	Rate coeff. $k = 3.734 \times 10^8 m^3/(s \cdot mol)$	[33,40]
R7: Ar(s) + Ar → Ar + Ar	Quenching	—	Rate coeff. $k = 1807 m^3/(s \cdot mol)$	[33,40]

is field driven rather than dominated by diffusion or ambipolar fields, the use of Townsend coefficients [41] for the evaluation of the ionization (R4) and excitation (R2) reaction rates for R_e and R_ε provide higher numerical stability and a quite accurate description of what happens in the cathode region, as shown in [43].

Employing the rate coefficients, k_j, the electron source term is given by $R_e = \sum_{j=1}^{M} \chi_j k_j n n_e$, while through the Townsend coefficients, a_j, it is given by $R_e = \sum_{j=1}^{M} \chi_j a_j n |\mathbf{\Gamma}_e|$. In these equations, χ_j is the mole fraction of the target species for reaction j, $\mathbf{\Gamma}_e$ is the electrons flux, n is the total neutral gas number density, and the index j here sums over all the reactions that contribute to the increase or loss of electrons. Correspondingly, the electron energy loss term is given by $R_\varepsilon = \sum_{j=1}^{L} \chi_j k_j n n_e \Delta_{\varepsilon_j}$ and $R_\varepsilon = \sum_{j=1}^{L} \chi_j a_j n |\mathbf{\Gamma}_e| \Delta_{\varepsilon_j}$, through k_j, and a_j, respectively, where Δ_{ε_j} (see Table 1) is the energy loss/gain from each reaction, and the index j here sums over all the electron-neutral inelastic collisions [34–36]. The detailed simulation procedure for the simulation of a DC plasma discharge via COMSOL can be found in ref. [36].

From Equations (4) and (5) one can see that a critical input parameter for the evaluation of the electron density is the mobility of the electrons, μ_e. The mobility, defined by $\mathbf{v}_e = \mu_e \mathbf{E}$, where $\mathbf{v}_e$ is the drift velocity and $\mathbf{E}$ the electric field, is closely connected also with the electrons collision frequency, ν, which is another critical frequency for the electromagnetic plasma response. For isotropic scattering it can be shown that [8]

$$\mu_e = \frac{e}{\nu_m m_e} \tag{7}$$

where $\nu_m = \nu/2\pi$. In our calculations, for obtaining the mobility (used as input in Equations (4) and (5)) we employed two different approaches: (a) Using values from the literature, and in particular the values by Raizer [8] and Trusov [44], which give the mobility as a function of the pressure in Torr, p_{torr}, as

$$\mu_e = 33/p_{\text{torr}}\ \text{m}^2/\text{Vs}\,(\text{Raizer}), \quad \mu_e = 27/p_{\text{torr}}\ \text{m}^2/\text{Vs}\,(\text{Trusov}) \tag{8}$$

(b) Evaluating the collision frequency and through it the mobility. For the evaluation of the collision frequency we based on the well-known collision formula $l = 1/n\sigma$, where l is the mean free path (mean space between successive collisions), n is the neutral gas number density and σ the electron-neutral collision cross-section, considered here as $\sigma = 3 \times 10^{-19}$ m^2 [37,45]. Given that $l = \bar{v}\tau_m = \bar{v}/\nu_m$ ($\tau_m = 1/\nu_m$ is the mean time between collisions) and that $\bar{v}$ is the average thermal velocity, which for plasmas obeying the Maxwellian distribution function (suitable for low pressure and weakly ionized gasses, as in our case) is $\bar{v} = \sqrt{8k_B T_e/\pi m_e}$ [46], one can derive for the collision frequency

$$\nu_m = n\sigma\bar{v} = \frac{p}{k_B T}\sigma\sqrt{\frac{8k_B T_e}{\pi m_e}} \tag{9}$$

where T is the neutral Ar temperature (room temperature in our case), and the electrons temperature T_e is obtained by COMSOL through the evaluation of electrons energy. Having the collision frequency, one can then calculate the mobility using Equation (7).

For $T_e = 11600K$ ($k_B T_e \approx 1$ ev) such a calculation gives $\mu_e \approx 27/p_{\text{torr}}$ m^2/Vs, which is in perfect agreement with the formulas provided in the literature.

We have to mention here that the above described multiphysics plasma modeling is a standalone, ab-initio approach, able to calculate from the microscopic plasma properties (reactions and species involved) and the plasma ignition system features (e.g. tube geometry, pressure, temperature, applied voltage/current, etc) the electron density and all the other macroscopic quantities determining the plasma response (electron temperature, velocity, etc.). This is particularly useful for the study of more complex and/or time-modulated plasma systems, as it enables the theoretical design and optimization of the plasma elements, minimizing unsuccessful experimental efforts. Given though the complexity of any plasma system and the different approximations involved in its simulation, validating the theoretical results through corresponding experimental or experimentally-driven data, as is done in this work, brings confidence to this multiphysics modeling approach and establishes it as a valuable tool for the plasma-metamaterials studies.

2.3 | Electric Characterization

The electrical characterization of the prototypes focuses on measuring their electrical behavior and estimating from the measurements results the plasma parameters, i.e. electron density and plasma frequency. The measurements are based on applied

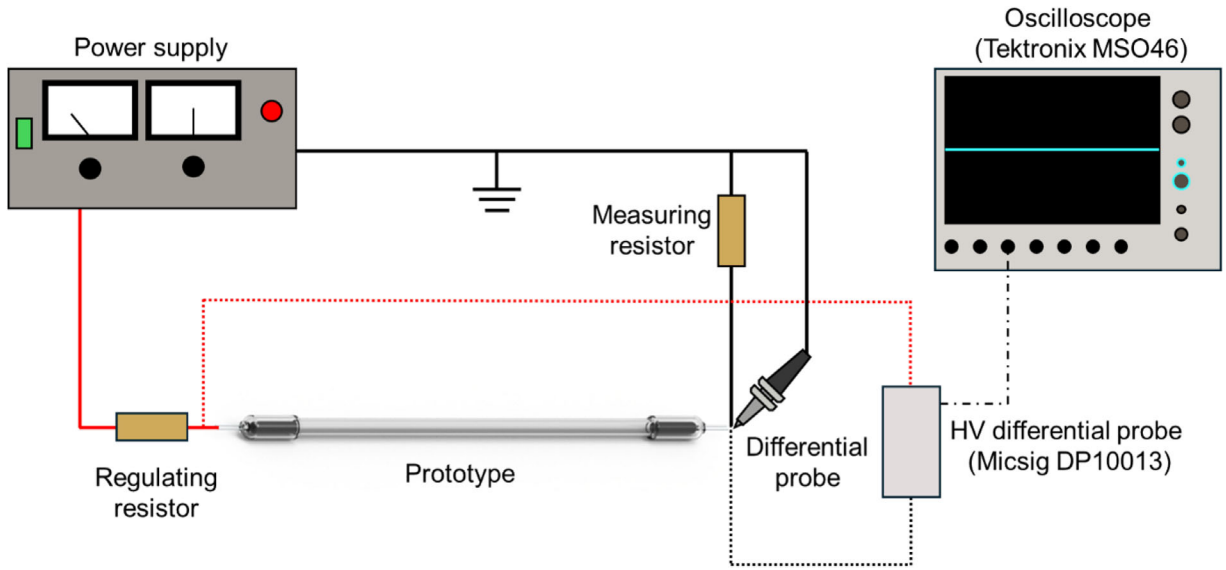

FIGURE 2 | Schematic diagram of the electric measurement setup.

voltage and current sampling under controlled conditions. The electrical operation of the prototype is dictated by the characteristics of the discharge tube (geometry, gas, pressure) and the external driving circuit/power supply.

A Heinzinger HNC 40 000 high-voltage generator (0–40 kV, 0–10 mA) is employed for plasma ignition, while a GW Instek ASR 2100 power supply (0–500 V, 0–5 A) provides controlled current boosts. The switching between sources is handled via diode-based OR logic. Current control is achieved through a resistive network composed of a regulating resistor (50–1000 Ω) and a measuring resistor. Voltage and current measurements are acquired using two probes connected to a Tektronix MSO46 oscilloscope. A Tektronix high-voltage probe measures the discharge voltage, while a second probe captures the current signal. A schematic of the measurement setup is shown in Figure 2.

Electron density n_e is estimated from the measured current I and calculated current density J, using the relation:

$$I = JA = n_e\, e\, v_e\, A$$

where v_e is the electron drift velocity ($v_e = \mu_e E$) and e is the elementary charge.

Pressure-dependent expressions for μ_e in Argon are obtained from literature sources (e.g., Raizer, Trusov).

Plasma frequency f_p is computed via the standard Drude expression:

$$f_p = \frac{\omega_p}{2\pi} = \frac{\sqrt{3180\, n_e}}{2\pi}$$

where ω_p is the frequency expressed in rad s^{-1}.

The electric field is calculated by dividing the measured discharge voltage by the inter-electrode distance, neglecting the sheath voltage drops. The cross-sectional area A is approximated using the tube diameter, acknowledging that plasma brightness impeded more precise evaluation.

These approximations tend to underestimate n_e and f_p, providing conservative lower bounds suitable for system design.

2.4 | Electromagnetic Characterization and Plasma Parameters Retrieval

The electromagnetic characterization of plasma tubes was designed around the idea that their presence within a controlled waveguide environment would introduce measurable perturbations to the transmitted and reflected microwave signals. By analyzing these effects (specifically, changes in the S-parameters) it is possible to infer key physical properties of the plasma, such as its electron density and plasma frequency. This approach forms the basis of the retrieval methodology employed in this work. The idea of using plasma discharges embedded in waveguide structures has been explored in several works, particularly for the realization of tunable filters and reconfigurable phase shifters at microwave frequencies [47–49]. These studies confirm that plasma tubes inserted into controlled propagation environments can enable frequency-selective behavior and phase modulation, motivating the use of similar setups for the parameter retrieval procedure of plasma tubes.

To this end, a custom measurement setup was developed, consisting of a WR90 rectangular waveguide section (dimensions: 22.86 mm x 10.16 mm) with a hole drilled through the wider wall to accommodate the insertion of a plasma tube along the centerline, oriented perpendicularly to the propagation axis in order to maximize interaction with the electric field of the dominant waveguide mode. The tube is externally excited for the ignition of the plasma, while its interaction with the guided mode is monitored via a vector network analyzer (model: Anritsu MS46122B with operating frequency range from 1 MHz to 43.5 GHz) connected to both ports of the waveguide, through a couple of right-angle rectangular waveguide to coaxial adapters. In

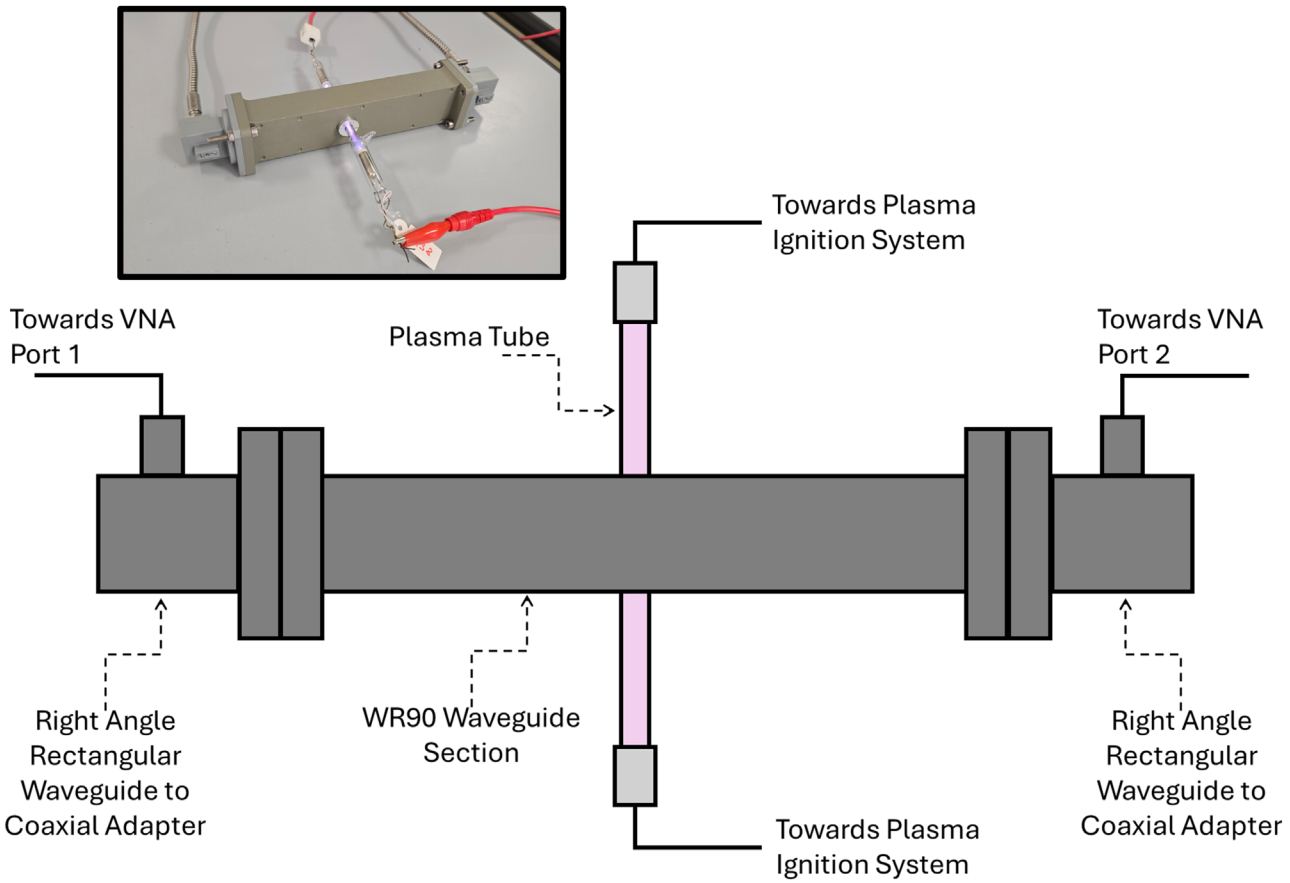

FIGURE 3 | Schematic representation of the measurement setup for the experimental characterization of the plasma tube. In the inset, a picture showing the ignited plasma tube in the waveguide measurement setup.

contrast to an open test setup, this configuration was chosen to ensure a well-defined, repeatable field distribution, and to minimize interfering effects that could obscure the plasma's contribution to the overall electromagnetic response. A schematic representation of the measurement setup used for the experimental characterization of the plasma tube, along with a photograph showing the ignited plasma tube within the waveguide measurement setup, is presented in Figure 3.

Under the assumption that all other properties of the system–namely, the geometry of the setup and the materials of the waveguide and the tube enclosure–are known and can be modeled with high fidelity, the plasma itself becomes the only unknown. This enables the use of a model-based parameter retrieval strategy, where the values of the plasma's electromagnetic parameters are adjusted within a full-wave simulation until the computed S-parameters match the measured ones.

To implement this approach, a finite-element method (FEM) electromagnetic model of the measurement setup was developed in CST Microwave Studio, as shown in Figure 4. The model replicates all relevant aspects of the experimental configuration, including the metallic boundaries of the waveguide, the dielectric characteristics of the glass tube (relative permittivity $\epsilon_r = 4.42$ and loss tangent $\tan\delta = 0.0034$, in accordance with the material specifications provided by the manufacturer), and the spatial positioning of the plasma column. The plasma is modeled as a

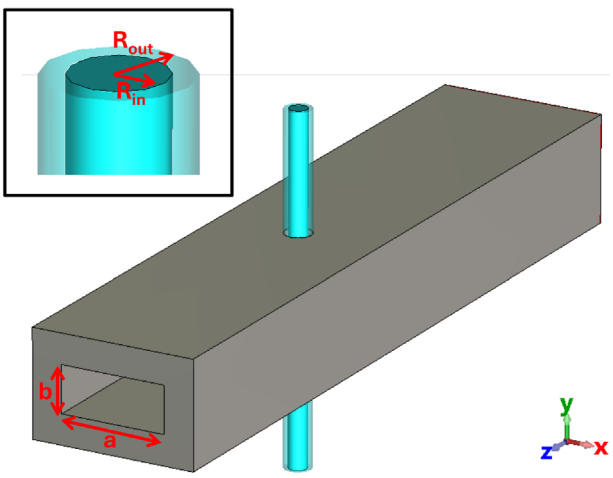

FIGURE 4 | Simulated setup for the retrieval of the main plasma characteristics. In the inset, a picture shows the radial dimensions of the plasma tube. Rectangular waveguide dimensions: $a = 22.86$ mm, $b = 10.16$ mm.

homogeneous, dispersive, and lossy medium described by the Drude model [30], as discussed in Section 2.2.

As can be seen in Equation (2), the plasma frequency is directly related to the square root of the electron density n_e, and it can

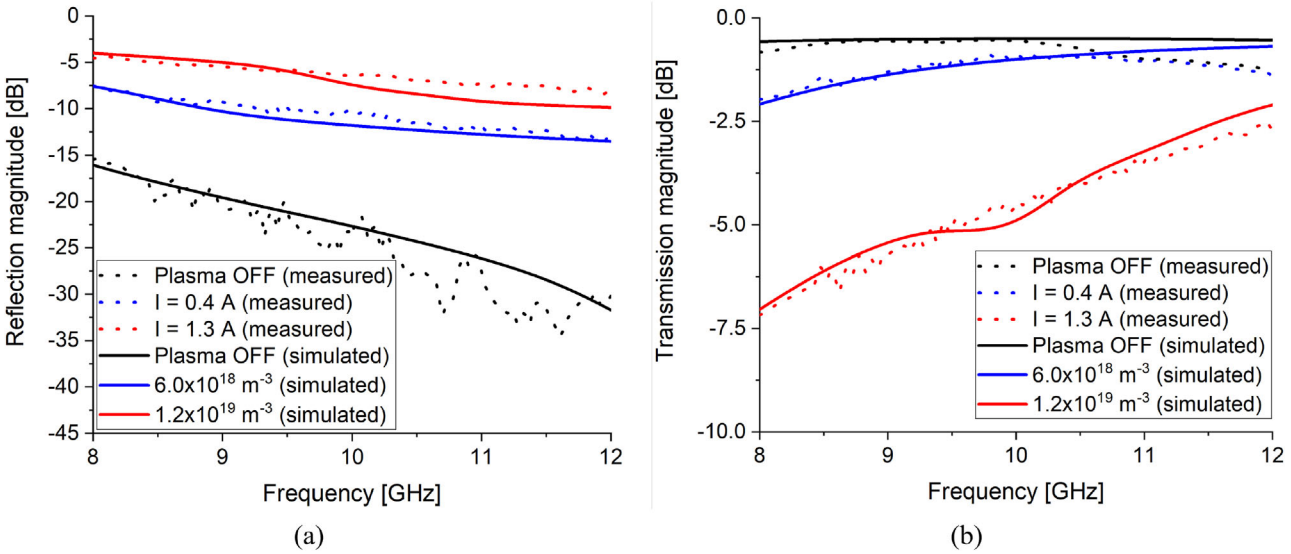

FIGURE 5 | Simulated and measured reflection (a) and transmission (b) magnitudes ($|S_{11}|$ and $|S_{21}|$) of the setups shown in Figures 3 and 4 for some representative plasma excitation levels.

be tuned over a wide range of values through external stimuli, i.e. by controlling the discharge power. In contrast, the collision frequency is influenced by the background gas pressure p and a temperature-dependent rate constant K that depends on the electron temperature and the gas species. For this reason, once the gas type and pressure are selected, we can fix ν to a representative value according to the literature (as verified in Section 2.2) and, under this assumption, extract the plasma frequency for different excitation conditions, as it becomes the only unknown parameter in the Drude model.

Simulations are performed over the same frequency range as the experimental measurements (8–12 GHz) using the frequency-domain solver in CST Microwave Studio. The model reproduces the WR90 waveguide geometry, with two waveguide ports exciting and receiving the dominant TE_{10} mode under matched boundary conditions. For each excitation condition (i.e., discharge current level), the model is calibrated to reproduce the measured transmission and reflection coefficients. This allows the estimation of the plasma frequency corresponding to each operating point. The comparison between simulated and measured reflection and transmission magnitudes ($|S_{11}|$ and $|S_{21}|$) for representative plasma excitation levels is reported in Figure 5, showing very good agreement and confirming the accuracy of the CST model in reproducing the experimental results.

Beyond parameter retrieval, the model also provides valuable physical insight into how the plasma affects the propagation of microwave energy, including frequency selectivity, absorption, and reflection characteristics. The analysis confirms that the plasma introduces a frequency-dependent and controllable perturbation that can be harnessed for a reconfigurable metasurface applications.

The accuracy of the electromagnetic model and its ability to reproduce the measured results are discussed in detail in Section 3, where the retrieved plasma parameters are compared with those obtained through independent electrical diagnostics.

3 | Results

The following subsections detail the results obtained through the three complementary approaches discussed in the previous section: multiphysics simulation of the plasma discharge, electrical characterization of the tube under current excitation, and full-wave electromagnetic modeling and plasma parameters retrieval. Their consistency validates the accuracy of the plasma description and confirms its suitability as a reconfigurable element for metasurface applications.

3.1 | Multiphysics Simulation Results

In this section, we present Multiphysics simulation results for the electron density and plasma frequency in the low pressure argon plasma tube investigated. The simulations were carried out by COMSOL Multiphysics software [33], following the procedure described in Section 2.2. For the modeling of a plasma tube as the one shown in Figure 1, selecting Ar as the plasma gas the software provides the chemical reactions involved in the plasma formation and the related reaction rates and coefficients. Required inputs, besides the neutral gas chemistry, are the applied current (I), the temperature (T), the pressure (p) and the electrons mobility. For the results shown here $T = 293.15$ K, $p = 0.75$ Torr and the mobility is obtained by the Raizer formula.

A two-dimensional cross-section schematic of the model system investigated through the multiphysics modeling is shown in Figure 6a, showing the different simulation domains and materials involved. The calculated electron density and plasma frequency are shown in Figure 6b–d.

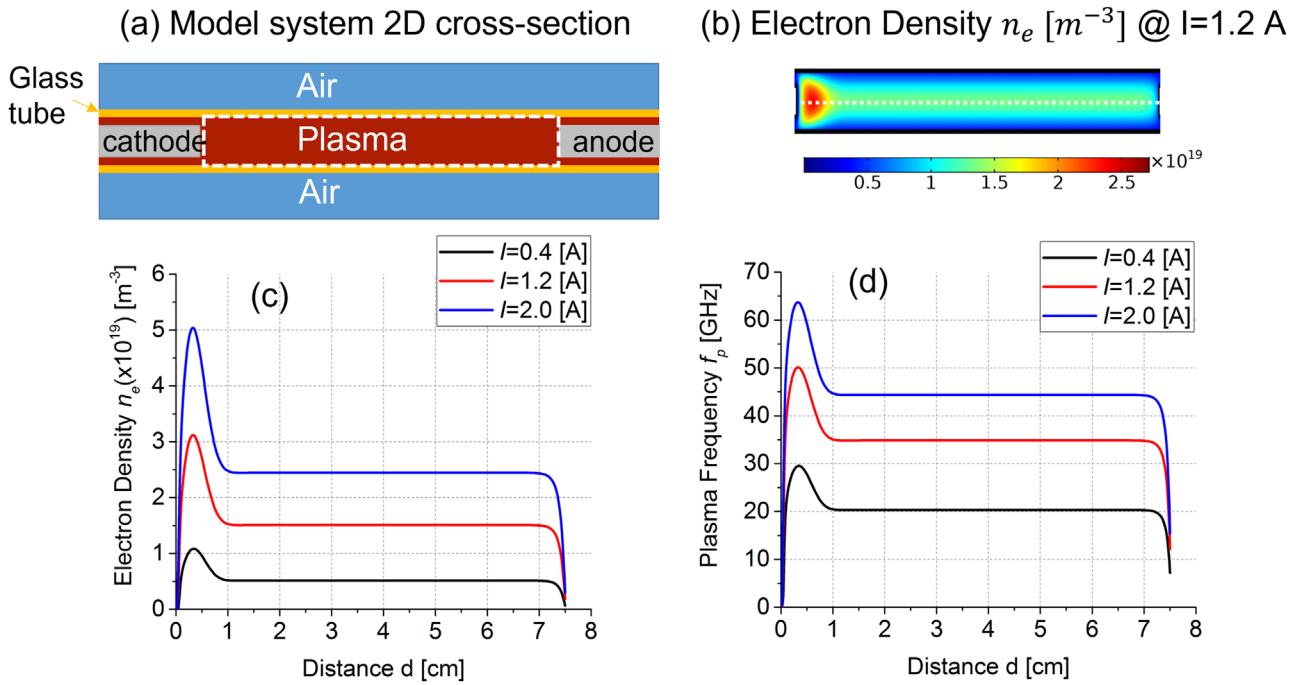

FIGURE 6 | Multiphysics simulations data for the electron density and plasma frequency for the plasma tube under investigation. (a) A 2D schematic of the simulation domain (rescaled vertically as to be more clearly visible). Note that in the simulations, given the rotational symmetry of the plasma tube system, a 2D axisymmetric model was employed (for computational time and memory reduction) involving only the upper half of the schematic shown. The white dashed-line rectangle shows the area over which the electron density is depicted in panel (b). (b) Electron density in the argon tube (in the domain indicated by the white dashed-line rectangle in (a)) when a current-source of $I = 1.2$ A (DC source) is applied for plasma ignition and for 0.75 Torr pressure. The white dotted-line shows the line over which the data of panels (c) and (d) are shown. Panel (c) shows the electron density, while panel (d) the corresponding plasma frequency along the white dotted-line of panel (b), for three values of applied current.

Specifically, Figure 6b presents the electron density distribution over a plasma tube cross-section (indicated by the white dashed-line rectangle in Figure 6a) when a DC source of current $I = 1.2$ A is applied. We observe a pronounced maximum of the electron density close to the cathode region, where the electron density gets values close to $n_e = 3 \times 10^{19}\ m^{-3}$, followed by a plateau as we go away from the cathode. To understand and quantify better the electron density distribution, in panels (c) and (d) of Figure 6 we show the electron density and the corresponding plasma frequency (calculated via Equation (2)) along the length of the tube (over a line passing from the center of the tube - white dotted line in panel (b)) for three different values of the applied current (low, medium, high). The results clearly demonstrate the broad peak close to the cathode, followed by a plateau away from the cathode region. Moreover, as expected, there is a clear increase of electron density as the applied current increases.

Additional simulation data concerning the electron density and plasma frequency for all the experimentally considered applied current values have been also obtained, and are presented in Table 2 and Figure 8, together with the corresponding experimental data obtained from both the electrical and the electromagnetic characterization approaches, demonstrating good agreement with those data and validating the COMSOL model and its results.

We should note here that the electron density simulation data presented in the Table 2 show the average value of the electron density along the dotted line of Figure 6b for each discharge current. The corresponding plasma frequency value is obtained employing this average electron density. In Figure 8, though, we show two different plasma frequency values for each discharged current. One is obtained using the maximum value of the electron density and one employing the average value mentioned above. Given the non-uniform electron density distribution over the tube, the averaged electron density may provide a more accurate estimation of the plasma frequency.

3.2 | Electrical Characterization and Parameter Extraction

Electrical diagnostics confirmed that the argon-filled prototypes can sustain a stable glow discharge across a wide range of driving conditions. The discharge current was found to scale predictably with the applied voltage and the resistor configuration, enabling controlled operation during measurements.

Using the relations described in Section 2.3, electron densities in the range of 10^{18} – $10^{19} m^{-3}$ were estimated, corresponding to plasma frequencies in the range 11–54 GHz. These values overlap well with those obtained from multiphysics simulations and electromagnetic measurements.

As discussed earlier, the simplifying assumptions of the electrical model, such as the use of the geometric cross-section, the neglect of the sheath voltage drops, and the assumption of uniform current distribution, make the method conservative. In practice,

TABLE 2 | Comparison of plasma density and plasma frequency values estimated using different methods.

I (A)	n_e Trusov (m^{-3})	n_e Raizer (m^{-3})	n_e retrieved (m^{-3})	n_e (num.) (m^{-3})	f_p Trusov (GHz)	f_p Raizer (GHz)	f_p retrieved (GHz)	f_p (num.) (GHz)
OFF	—	—	—	—	—	—	—	—
0.40	2.38×10^{18}	1.66×10^{18}	$\sim 7.00 \times 10^{18}$	5.18×10^{18}	13.85	11.86	~ 23.8	21.07
0.50	3.53×10^{18}	2.46×10^{18}	$\sim 8.50 \times 10^{18}$	6.91×10^{18}	16.87	14.08	~ 26.2	23.37
0.60	6.88×10^{18}	4.79×10^{18}	$\sim 9.00 \times 10^{18}$	8.23×10^{18}	23.54	19.65	~ 26.9	25.53
0.70	1.01×10^{19}	7.06×10^{18}	$\sim 9.50 \times 10^{18}$	9.45×10^{18}	28.56	23.84	~ 27.7	27.44
0.80	1.25×10^{19}	8.68×10^{18}	$\sim 1.00 \times 10^{19}$	1.07×10^{19}	31.68	26.45	~ 28.4	29.29
0.90	1.27×10^{19}	8.86×10^{18}	$\sim 1.05 \times 10^{19}$	1.21×10^{19}	32.00	26.72	~ 29.1	30.91
1.00	1.41×10^{19}	9.85×10^{18}	$\sim 1.10 \times 10^{19}$	1.34×10^{19}	33.73	28.16	~ 29.8	32.7
1.10	1.71×10^{19}	1.19×10^{19}	$\sim 1.10 \times 10^{19}$	1.48×10^{19}	37.15	31.01	~ 29.8	34.35
1.20	1.87×10^{19}	1.30×10^{19}	$\sim 1.15 \times 10^{19}$	1.62×10^{19}	38.80	32.39	~ 30.5	35.88
1.30	2.39×10^{19}	1.67×10^{19}	$\sim 1.20 \times 10^{19}$	1.75×10^{19}	43.90	36.65	~ 31.1	37.56
1.40	2.58×10^{19}	1.80×10^{19}	$\sim 1.30 \times 10^{19}$	1.88×10^{19}	45.56	38.04	~ 32.4	38.67
1.50	2.76×10^{19}	1.92×10^{19}	$\sim 1.50 \times 10^{19}$	2.01×10^{19}	47.16	39.37	~ 34.8	40.01
1.60	2.96×10^{19}	2.05×10^{19}	$\sim 1.70 \times 10^{19}$	2.13×10^{19}	48.71	40.66	~ 37.0	41.15
1.70	3.13×10^{19}	2.18×10^{19}	$\sim 1.75 \times 10^{19}$	2.25×10^{19}	50.21	41.92	~ 37.6	42.38
1.80	3.31×10^{19}	2.31×10^{19}	$\sim 1.75 \times 10^{19}$	2.37×10^{19}	51.66	43.13	~ 37.6	43.52
1.90	3.50×10^{19}	2.44×10^{19}	$\sim 1.80 \times 10^{19}$	2.55×10^{19}	53.08	44.31	~ 38.1	44.65
2.00	3.68×10^{19}	2.57×10^{19}	$\sim 1.90 \times 10^{19}$	2.62×10^{19}	54.46	45.46	~ 39.1	46.07

the effect is most evident at low discharge currents, where sheath effects are more pronounced and the plasma is less uniform. At higher currents, the plasma fills a larger portion of the tube volume, reducing the discrepancy and bringing the electrical estimates closer to those obtained from multiphysics simulations and electromagnetic retrieval.

Although approximate, the electrical characterization provides a rapid and a reliable way to track the evolution of plasma parameters with current. This makes it particularly useful for monitoring discharge conditions and for providing first-order validation of the more detailed numerical and electromagnetic models.

Representative operating points are summarized in Table 2.

3.3 | Electromagnetic Response and Drude Model Validation

The electromagnetic characterization, as discussed in Section 2.4, relied on reflection and transmission measurements in the WR90 waveguide setup, complemented by the corresponding CST simulations. A baseline "plasma-off" condition was first measured to calibrate systematic mismatches. Then, for each discharge current level, the plasma frequency was retrieved by adjusting the Drude model in CST simulations until the measured and simulated S-parameters matched at 9.5 GHz, chosen as a reference within the waveguide band.

Assuming a fixed collision frequency $\nu = 1.65 \times 10^{10}$ Hz for argon at 1 mbar, the retrieval yielded plasma frequencies that increased monotonically with discharge current.

Figure 8 illustrates the good agreement with both analytical models (Raizer, Trusov) and multiphysics simulations. Slight deviations are attributed to non-idealities neglected in the Drude model, such as axial non-uniformities and sheath effects.

Despite these simplifications, the results confirm that a single-parameter Drude description can accurately reproduce the plasma's electromagnetic behavior in the X-band, making it a practical model for metasurface integration.

To demonstrate the applicability of the characterized plasma tubes as tunable elements for reconfigurable metasurfaces, we applied the numerical framework previously discussed in [25, 26] to the experimental case investigated in this work. Specifically, a unit-cell analysis was carried out using CST Microwave Studio to evaluate the free-space response of a periodic arrangement of plasma tubes. It is important to note that the following results refer to the phase shift of a periodic array of tubes under plane-wave excitation, and should not be confused with the waveguide configuration discussed earlier in the paper, which was used for the retrieval of the plasma frequency. The geometry of the unit cell consists of a single plasma tube periodically repeated with a representative period p_c, as shown in Figure 7a. The plasma region is modeled as a homogeneous dispersive medium described by the Drude model, where the plasma frequency f_p is varied within the range extracted from the experimental and numerical characterizations. The transmission amplitude and phase of the unit cell were evaluated at a fixed frequency of 9.5 GHz for both TE and TM polarizations, considering a single-layer configuration with a representative lattice period $p_c = 15\ mm$. The results, reported in Figure 7b, shows the evolution of the transmission coefficient (magnitude and phase) as a function of f_p. As the plasma frequency increases, a clear phase variation is observed, confirming the tunable electromagnetic response of the plasma element and its suitability as a dynamic meta-atom for reconfigurable and programmable metasurfaces. Although this analysis was limited to a single-layer periodic configuration, further improvements in phase coverage and transmission control could be achieved through multi-layer designs or by optimizing the lattice period and geometric parameters of the unit cell [26]. These aspects, however, go beyond the scope of the present work.

3.4 | Comparison and Discussion

Table 2 and Figure 8 summarize the electron density n_e and plasma frequency f_p obtained with the three complementary approaches: (i) electrical diagnostics, (ii) multiphysics plasma simulations, and (iii) electromagnetic retrieval from waveguide measurements.

The comparison highlights several key points:

- All three approaches indicate that the plasma tube exhibits tunable electron densities in the order of 10^{18}–$10^{19}\ m^{-3}$, corresponding to plasma frequencies tunable between 10 and 40 GHz as the discharge current increases from 0.4 to 2.0 A. This range is compatible for reconfigurable metadevices operating at least up to the X-band, as suggested by the numerical results of recent designs reported in the literature [25–28] and by the preliminary unit-cell analysis previously reported.
- At low discharge currents, the electrical model, which assumes a uniform conduction area and neglects sheath voltage drops, tends to underestimate n_e and f_p. As the current increases, the discrepancy diminishes, leading to close agreement with the multiphysics and electromagnetic retrievals. At the highest currents, deviations can even change sign depending on the actual evolution of electron temperature and mobility (when literature-based mobilities are no longer representative). Overall, the electrical approach remains a fast, first-order estimator for design iteration.
- The COMSOL-based fluid model captures spatial distributions of plasma density and temperature. It predicts non-uniform electron density profiles along the tube, with values which agree well with experimental trends. The model also enables parametric studies beyond the experimentally accessible regime (e.g., higher currents or different gases).
- The waveguide-based method provides the most application-oriented parameters, since it directly connects the plasma behavior with the S-parameters relevant for metasurface design. The retrieved f_p values follow a monotonic increase with discharge current and match the simulations and analytical models within 10–15% across the tested range.

Some deviations are observed at higher currents ($I > 1.5$ A), where electromagnetic retrieval yields slightly lower plasma

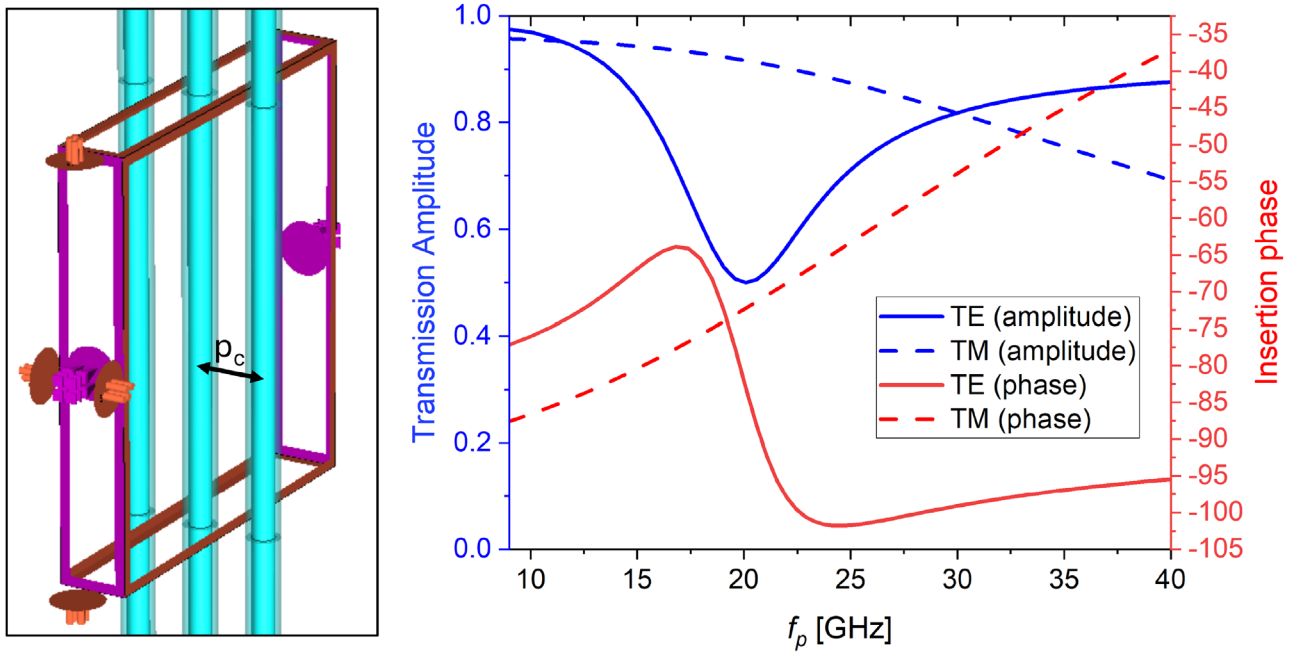

FIGURE 7 | (a) Geometry of the simulated periodic unit cell including a plasma tube, modeled in CST Microwave Studio with periodic boundary conditions; (b) Simulated transmission amplitude and phase evaluated at 9.5 GHz under TE and TM polarizations as a function of the plasma frequency f_p. The results demonstrate a clear phase tunability consistent with the f_p values retrieved experimentally.

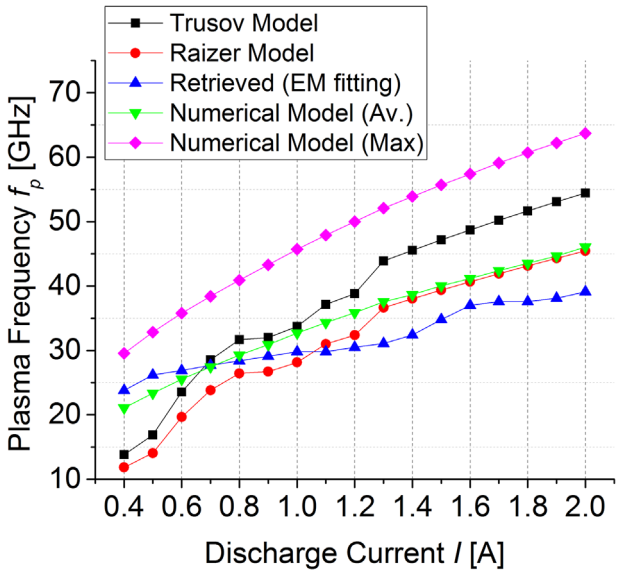

FIGURE 8 | Comparison of plasma frequency f_p as a function of discharge current I, estimated using the models of Trusov and Raizer, retrieved from full-wave electromagnetic simulations and a numerical plasma model. For the numerical model the plasma frequency is obtained using both the peak value and the averaged (over the tube volume) value of the electron density.

frequencies than the Raizer and Trusov models. This discrepancy can be attributed to (i) the assumption of spatial uniformity in the Drude model, (ii) temperature gradients along the discharge, (iii) sheath effects near the electrodes, and (iv) a saturation effect in the retrieval procedure that is limited in frequency by the operating band of the waveguide.

Despite these differences, all approaches yield consistent monotonic trends of n_e and f_p with increasing discharge current, and provide values within the same order of magnitude, which is remarkable given that direct, localized measurements of electron density in this pressure and geometry range are notoriously difficult. Moreover, the error remains within acceptable bounds for engineering purposes, since the discharge current could be optimized experimentally to produce the desired electromagnetic response, with operating points (i.e. discharge currents) expected to remain close to the experimentally characterized interval.

Overall, the complementary use of electrical, multiphysics, and electromagnetic models provide a robust framework for plasma characterization. The agreement among these independent approaches confirms that plasma tubes offer a continuously tunable, controllable, and predictable electromagnetic response in the X-band, making them promising candidates for reconfigurable and programmable metasurface applications.

4 | Conclusion

This work has presented a comprehensive study of plasma tubes as reconfigurable building blocks for programmable metasurfaces. Through the combined use of electrical diagnostics, multiphysics plasma simulations, and full-wave electromagnetic retrieval, we have consistently characterized the plasma response under different excitation conditions.

The results confirm that plasma tubes can provide a controllable and predictable electromagnetic behavior in the microwave regime, validating their potential use as dynamic meta-atoms for adaptive metasurface architectures at least up to the X-band,. The agreement among the three independent approaches demonstrate the robustness of the characterization framework and the reliability of a Drude-based description for practical design purposes.

Although a complete metasurface prototype was not realized in this work, the findings represent a fundamental step toward that goal. Future research will address the integration of plasma tubes into large-scale metasurfaces, exploring functionalities such as beam steering, reconfigurable focusing, and programmable holography. Additional directions include extending the concept to higher frequency bands and exploiting the intrinsic high-power handling capability of plasmas in regimes where conventional electronic tuning elements face limitations.

In conclusion, this study establishes plasma tubes as viable candidates for the realization of reconfigurable and programmable metasurfaces, paving the way toward future developments in high-speed, high-power, and dynamically tunable electromagnetic platforms.

Acknowledgements

This work has been developed in the framework of the activities of the Project PULSE, funded by the European Innovation Council under the EIC Pathfinder Open 2022 program (protocol number 10109931).

Conflicts of Interest

The authors declare no conflicts of interest.

Data Availability Statement

The data that support the findings of this study are available from the corresponding author upon reasonable request.

References

1. T. Gu, H.-J. Kim, C. Rivero-Baleine, et al., "Reconfigurable Metasurfaces Towards Commercial Success," *Nature Photonics* 17 (2023): 48–58.

2. Z. Zhang, H. Shi, L. Wang, et al., "Recent Advances in Reconfigurable Metasurfaces: Principle and Applications," *Nanomaterials* 13, no. 3 (2023): 534.

3. M. Barbuto, Z. Hamzavi-Zarghani, M. Longhi, et al., "Metasurfaces 3.0: A new Paradigm for Enabling Smart Electromagnetic Environments," *IEEE Transactions on Antennas and Propagation* 70, no. 10 (2022): 8883–8897.

4. D. Ramaccia, A. Monti, M. Barbuto, et al., "Reconfigurability in Electromagnetic Metasurfaces and Metamaterials for Antennas Systems: State-of-the-art, Technical Approaches, Limitations, and Application," *IEEE Antennas and Propagation Magazine* (2025), in press.

5. A. Komar, Z. Fang, J. Bohn, et al., "Electrically Tunable All-Dielectric Optical Metasurfaces Based on Liquid Crystals," *Applied Physics Letters* 110, no. 7 (2017): 071109.

6. M. Kim, J. Jeong, J. K. S. Poon, and G. V. Eleftheriades, "Vanadium-Dioxide-Assisted Digital Optical Metasurfaces for Dynamic Wavefront Engineering," *Journal of the Optical Society of America B* 33, no. 5 (2016): 980–988.

7. C. Choi, S.-Y. Lee, S.-E. Mun, et al., "Metasurface with Nanostructured ge2sb2te5 as a Platform for Broadband-Operating Wavefront Switch," *Advanced Optical Materials* 7, no. 12 (2019): 1900171.

8. Y. P. Raizer, *Gas Discharge Physics* (Springer, 1991).

9. K. Kourtzanidis, D. M. Pederson, and L. L. Raja, "Electromagnetic Wave Energy Flow Control with a Tunable and Reconfigurable Coupled Plasma Split-Ring Resonator Metamaterial: A Study of Basic Conditions and Configurations," *Journal of Applied Physics* 119, no. 20 (2016): 204904.

10. K. Payne, K. Xu, J. H. Choi, and J. K. Lee, "Electrically Tunable Microwave Absorber Based on Discrete Plasma-Shells," *IEEE Transactions on Antennas and Propagation* 67, no. 10 (2019): 6523–6531.

11. K. Kourtzanidis and L. L. Raja, "Analysis and Characterization of Microwave Plasma Generated with Rectangular All-Dielectric Resonators," *Plasma Sources Science and Technology* 26, no. 4 (2017): 045007.

12. A. Simon, R. Pascaud, T. Callegari, L. Liard, and O. Pascal, "Experimental Study of Microwave Power Limitation in a Microstrip Transmission Line Using a dc Plasma Discharge for Preionization," *IEEE Transactions on Plasma Science* 46, no. 7 (2018): 2512–2520.

13. F. Pizarro, P. Stuardo, R. Olivares, and E. Rajo-Iglesias, "Potential Use of Cold Plasma Discharges for Frequency Reconfigurability in a Sievenpiper Mushroom Metasurface," *Applied Sciences* 11, no. 23 (2021): 11342.

14. M. Magarotto, L. Schenato, M. Santagiustina, A. Galtarossa, A.-D. Capobianco, "Plasma-Based Reflecting and Transmitting Surfaces," *IEEE Access* 11 (2023): 91196–91205.

15. B. Wang and M. Cappelli, "A Tunable Microwave Plasma Photonic Crystal Filter," *Applied Physics Letters* 107, no. 17 (2015): 171107.

16. P. Linardakis, G. Borg, and N. Martin, "Plasma-Based Lens for Microwave Beam Steering," *Electronics Letters* 42 (2006): 444–446.

17. A. D. Dotto, E. Chiadroni, A. Cianchi, et al., "Compact and Tunable Active-Plasma Lens System for Witness Extraction and Driver Removal," *Journal of Physics: Conference Series* 1596, no. 1 (2020): 012050.

18. G. G. Borg, J. H. Harris, N. M. Martin, et al., "Plasmas as Antennas: Theory, Experiment and Applications," *Physics of Plasmas* 7, no. 5 (2000): 2198–2202.

19. R. Pascaud, V. Laquerbe, A. Laffont, et al., "Towards Antenna Miniaturization at Radio Frequencies Using Plasma Discharges," *Physics of Plasmas* 26, no. 3 (2019): 033509.

20. D. Melazzi, P. De Carlo, F. Trezzolani, M. Manente, A.-D. Capobianco, and S. Boscolo, "Beam-Forming Capabilities of a Plasma Circular Reflector Antenna," *IET Microwaves, Antennas & Propagation* 12, no. 15 (2018): 2301–2306.

21. I. Alexeff, T. Anderson, S. Parameswaran, E. Pradeep, J. Hulloli, and P. Hulloli, "Experimental and Theoretical Results with Plasma Antennas," *IEEE Transactions on Plasma Science* 34, no. 2 (2006): 166–172.

22. C. Wang, B. Yuan, W. Shi, and J. Mao, "Low-Profile Broadband Plasma Antenna for Naval Communications in Vhf and Uhf Bands," *IEEE Transactions on Antennas and Propagation* 68, no. 6 (2020): 4271–4282.

23. K. Kanth Varikuntla, M. Ali Babar Abbasi, and O. Yurduseven, "Reconfigurable Plasma Frequency Selective Surface," in *2025 URSI Int. Symp. on Electromagnetic Theory (EMTS)* (2025), 1–4.

24. T. R. Jones, A. Fisher, and D. Peroulis, "Experimental Investigation of a Photogenerated Silicon Plasma Monopole Antenna," *IEEE Transactions on Antennas and Propagation* 70, no. 12 (2022): 11 353–11 360.

25. A. Monti, S. Vellucci, M. Barbuto, et al., "Design of Reconfigurable Huygens Metasurfaces Based on Drude-Like Scatterers Operating in the Epsilon-Negative Regime," *Optics Express* 32 (2024): 28 429–28 440.

26. J. Yan, I. Katsantonis, I. Draganidis, et al., "Reconfigurable Metasurface Based on Plasma Cylinders," *Physical Review Research* 7 (2025): 013287.

27. M. G. H. Alijani, A. Monti, S. Vellucci, M. Barbuto, A. Toscano, and F. Bilotti, "Design of Tunable Diffraction Meta-Gratings Based on Plasma Discharges," *IEEE Access* 13 (2025): 2169–3536.

28. M. G. H. Alijani, A. Monti, S. Vellucci, M. Barbuto, A. Toscano, and F. Bilotti, "Tunable Transmissive Metagratings Using Single Layer Cylindrical Plasma Discharges," *IEEE Antennas and Wireless Propagation Letters* (2025): 1–5.

29. E. V. Shun'ko, *Langmuir Probe in Theory and Practice* (Universal Publishers, 2009).

30. G. Colonna and A. D'Angola, eds., *Plasma Modeling (Second Edition)*, ser. 2053-2563 (IOP Publishing, 2022).

31. J. A. Bittencourt, *Fundamentals of Plasma Physics*, 3rd ed. (Cham, Switzerland: Springer, 2013).

32. A. A. D. Tereshonok, T. Chernyshev and A. Ugryumov, "The Comparison of Two-Term Boltzmann Approximation and Monte-Carlo Solutions for e+ar0 Plasma," *Physica Scripta* 98 (2023): 055602.

33. COMSOL, "Comsol Multiphysics," https://www.comsol.com/plasma-module.

34. COMSOL, "The Plasma Module User's Guide," https://doc.comsol.com/5.4/doc/com.comsol.help.plasma/PlasmaModuleUsersGuide.pdf.

35. COMSOL, "Introduction to the Plasma Module," https://doc.comsol.com/5.5/doc/com.comsol.help.plasma/IntroductionToPlasmaModule.pdf.

36. COMSOL, "Dc Glow Discharge," https://www.comsol.com/model/dc-glow-discharge-8640.

37. Phelps, "Phelps Database," https://www.lxcat.net.

38. K. Kourtzanidis, G. Dufour, and F. Rogier, "Self-Consistent Modeling of a Surface ac Dielectric Barrier Discharge Actuator: in-Depth Analysis of Positive and Negative Phases," *Journal of Physics D: Applied Physics* 54, no. 4 (2020): 045203.

39. K. Kourtzanidis and S. M. Starikovskaia, "Spatiotemporal Dynamics of Nanosecond Pulsed Discharge in the Form of a Fast Ionization Wave: Self-Consistent Two-Dimensional Modeling and Comparison with Experiments Under Negative and Positive Polarity," *Journal of Physics D: Applied Physics* 58, no. 19 (2025): 195202.

40. D. Lymberopoulos and D. Economou, "Fluid Simulations of Glow-Discharges - Effect of Metastable Atoms in Argon," *Journal of Applied Physics* 73, no. 8 (1993): 3668–3679.

41. J. R. Losee and D. S. Burch, "Experimental Electron Energy Distributions for Townsend Discharges in Argon Gas," *Physical Review A* 6 (1972): 1652.

42. Y. Che, Q. Zang, X. Han, et al., "Two-Dimensional Simulation of an Ar/H2 Direct-Current Discharge Plasma," *AIP Advances* 11, no. 5 (2021): 055209.

43. M. Lieberman and A. Lichtenberg, *Principles of Plasma Discharges and Materials Processing* (John Wiley & Sons, 2005).

44. K. K. Trusov, "Dynamics of Multichannel and Quasihomogeneous Sliding Discharge Formation in Rare Gases," *Journal of Physics D: Applied Physics* 40 (2007): 786–794.

45. LXCat Project Database.

46. The average electron velocity (magnitude), $\bar{v}$, can be calculated from the Maxwellian distribution function $f(v) = \sqrt{\frac{2}{\pi}}(\frac{m_e}{k_B T_e})^{3/2} v^2 e^{-mv^2/2k_B T_e}$, as $\bar{v} = \int_0^\infty v f(v) dv$. The distribution function $f(v)$ is obtained by the standard Maxwell–Boltzmann distribution function, $f(\mathbf{v})$, in 3D, after decomposition is spherical coordinates. $v = |\mathbf{v}|$.

47. A. Rezagholi and F. Mohajeri, "Construction, Simulation, and Experimental Verification of a Gas-Discharge Plasma Waveguide Phase Shifter," *AEU - International Journal of Electronics and Communications* 108 (2019): 195–205.

48. A. Ashrafian, F. Sadeghikia, J. A. Rashed Mohassel, M. Himdi, and M. Magarotto, "Tunable Rectangular Waveguide Bandpass Filter Based on Plasma Technology," in *2024 18th European Conf. on Antennas and Propagation (EuCAP)* (2024), 1–4.

49. V. I. Arkhipenko, T. Callegari, L. V. Simonchik, J. Sokoloff, and M. S. Usachonak, "One-Dimensional Electromagnetic Bandgap Structures Formed by Discharge Plasmas in a Waveguide," *Journal of Applied Physics* 116, no. 12 (2014): 123302.